PRECISION MEASUREMENT OF THE NEUTRON SPIN STRUCTURE FUNCTION.

Robert C. Welsh*
Physics Department,
The University of Michigan
Ann Arbor, MI 48109

Representing the SLAC E154 Collaboration

ABSTRACT

Deep Inelastic Scattering of electrons has been used for nearly three decades to probe the internal structure of nucleons. The vast majority of the available data on deep inelastic scattering comes from unpolarized experiments. These experiments have revealed the internal linear momentum structure of nucleons. However, not until the last decade and a half have experiments been carried out to elucidate the internal angular momentum structure of the nucleons. Recently the experiment E154 at the Stanford Linear Accelerator Center has completed a two month data taking run in which a large number ($\sim 10^8$) of spin–dependent deep inelastic scattering events were collected. The experiment covered the kinematic range of $0.014 \leq x \leq 0.70$ and $1\ (\mathrm{GeV/c})^2 \leq Q^2 \leq 17\ (\mathrm{GeV/c})^2$. The preliminary analysis of these data yield to date the most precise integral of $\int_{0.014}^{0.70} g_1^n(x)\ dx = -0.036 \pm 0.004(\mathrm{statistical}) \pm 0.005(\mathrm{systematic})$ at an average Q^2 of $5\ (\mathrm{GeV/c})^2$.

*Supported by NSF Grant PHY–9515418.

1 Introduction

1.1 Spin–averaged Deep Inelastic Scattering

Deep Inelastic Scattering (DIS) experiments take advantage of the point–like nature and the relatively weak electro–magnetic interaction of leptons to probe the internal structure of hadrons, specifically nucleons. I will speak mainly of electrons except when referring to other experiments such as the muon scattering experiments at CERN. In deep inelastic scattering experiments a high energy lepton beam impinges upon a nuclear target. The energy and momentum transfer to the target nucleon can be calculated by detecting scattered electron and measuring its momentum. Experiments from the late 1960's established the parton model as a description of DIS. The 1990 Nobel Prize in Physics was awarded for these seminal experiments.[?,?,?] Further experimentation led to the observation of *Scale Invariance* as predicted by Bjorken[?] and the explanation of scaling in the context of the parton model by Feynman.[?]

The parton model lets the experimenter equate the fraction x of the momentum of the nucleon carried by the struck parton (quark) to a ratio of kinematic observables,

$$x = \frac{-q^2}{2\ M_{\mathrm{N}}\ \nu}\ , \tag{1}$$

where q^2 is the four–momentum transfer squared, $\nu = E - E'$ is the energy transfer, and M_{N} is the nucleon mass. In the Born approximation, the scattering is described by single photon exchange between the incoming lepton and the struck quark. This is schematically shown in Figure 1. The internal momentum structure of the nucleon can be extracted from the x dependence of the scattering rates and summarized in the *structure functions*, $F_1(x)$ and $F_2(x)$.

In the years subsequent to the original DIS experiments the theory of *Quantum Chromodynamics* (QCD) has become a good description of the dynamics of partons (quarks and gluons). QCD[?,?,?] has been quite successful in explaining the dynamics of scale violation in parton distributions.[?] Currently high precision data for the spin–averaged nucleon structure functions[?] are available and provide for a rigorous test of QCD. However, only recently have high precision data for *spin–dependent* structure functions become available.

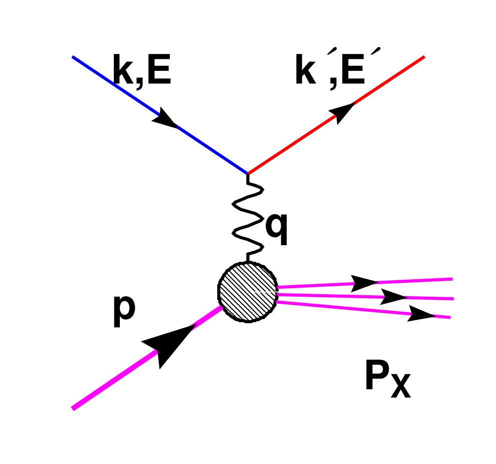

k, E	incoming electron
k', E'	scattered electron
$q^2 = (k-k')^2 = -4EE'\sin^2\frac{\theta}{2}$	
p	initial nucleon momentum
P_x	unobserved final hadron momentum

Fig. 1. Schematic of Deep Inelastic Scattering

1.2 Spin–Dependent DIS

The impetus for spin–dependent DIS is the desire to fully understand and describe the spin nature of the nucleon. We know from low Q^2 measurements that the nucleon is a spin 1/2 particle. From the parton description we also know that the nucleon is comprised of spin 1/2 (quarks) and spin 1 (gluons) particles. From angular momentum conservation we then can put forth the following

$$S_{\text{nucleon}} \equiv \frac{1}{2} = \frac{1}{2}\Delta q + \Delta G + <L> \; , \tag{2}$$

where Δq is the portion of the nucleon's spin carried by the quarks, ΔG that carried by the gluons and $<L>$ the internal orbital angular momentum.

This current experiment undertook the task of precisely measuring the neutron spin–dependent structure function $g_1^n(x)$[1]. To first order the measurement of the spin–dependent structure function $g_1(x)$ is a probe of the longitudinal quark spin content of the nucleon. Since free neutrons are unstable and the use of a neutron beam from a facility such as a reactor is impractible, preparation of a polarized neutron target requires the use of either a deuterated molecule, such as ND_4 or Butonal, or a nucleus in which an unpaired neutron can be effectively polarized, such as ^{3}He. A rather good approximation of the ^{3}He wave–function is that the two protons are paired off as a spin singlet and the unpaired neutron carries the spin of the nucleus. More exact treatments[?] show that the neutron polarization is $P_n = 0.87$ and the proton polarization is $P_p = -0.027$. Thus,

[1]Data primarily sensitive to $g_2^n(x)$ were also collected.

spin dependence is dominated by the neutron; while in the deuteron, the proton and the neutron have spins aligned. Measurement of the neutron spin–dependent structure function using the deuteron requires the subtraction of 100% of the proton spin structure function. Extraction of the neutron spin structure from deep inelastic data taken with ^{3}He targets requires a much smaller adjustment due to the proton contribution, though the asymmetry is smaller. The experiment E154 used polarized ^{3}He for the present measurement of the neutron spin structure.

Spin–dependent DIS is described by the following differential cross–section[?]

$$\begin{aligned}\frac{d\sigma}{dE'd\Omega} &= 4E'^2\frac{\alpha^2}{Q^2}\left[2\sin^2\left(\frac{\theta}{2}\right)W_1(Q^2,\nu)+\cos^2\left(\frac{\theta}{2}\right)W_2(Q^2,\nu)\right] \\ &\quad -\frac{E'\alpha^2}{EQ^4}\left[\frac{2m_e\left[q^2\ S_P\cdot S_e - q\cdot S_e\ q\cdot S_p\right]}{P\cdot q}g_1(x,Q^2)\right. \\ &\quad \left. +\frac{2m_e\left[q^2\left(q\cdot P\ S_p\cdot S_e - q\cdot S_p\ P\cdot S_e\right)\right]}{(P\cdot q)^2}g_2(x,Q^2)\right] \end{aligned} \tag{3}$$

The four–momentum transfer is q, the target nucleon four–momentum is P, and the beam and target polarization four–vectors are S_e and S_p respectively. Under change of sign of the beam helicity, the four–vector S_e changes overall sign. The differences in spin–dependent cross–sections for the cases a) the spins of the incoming electron and nuclear target are parallel and anti–parallel and b) the spins of the incoming electron and the nuclear target are perpendicular and anti–perpendicular are

$$\begin{aligned}(a)\quad \frac{d^2\sigma(\downarrow\Uparrow - \uparrow\Uparrow)}{d\Omega dE'} &= \frac{4\alpha^2 E'}{EM\nu Q^2}\left([E+E'\cos\theta]g_1(x) - 2xMg_2(x)\right) \\ (b)\quad \frac{d^2\sigma(\downarrow\Leftarrow - \uparrow\Leftarrow)}{d\Omega dE'} &= \frac{4\alpha^2 E'}{EM\nu Q^2}E'\sin\theta\left(g_1(x)+\frac{4xME}{Q^2}g_2(x)\right)\end{aligned} \tag{4}$$

In the scaling limit the spin–dependent structure function $g_1(x)$ can be shown to be the difference of spin–dependent parton distributions

$$g_1(x) = \frac{1}{2}\sum_{\text{Flavors }(i)} q_i^2\left(f_i^{\uparrow}(x) - f_i^{\downarrow}(x)\right)\ , \tag{5}$$

where the charge of the parton (quark) is given by q_i. The i^{th} partonic structure function is denoted by f_i. Likewise, the spin–averaged structure function is the average of the spin–dependent parton distributions

$$F_1(x) = \frac{1}{2}\sum_{\text{Flavors }(i)} q_i^2\left(f_i^{\uparrow}(x) + f_i^{\downarrow}(x)\right)\ . \tag{6}$$

Furthermore, the individual spin–dependent structure functions $g_1(x)$ and $g_2(x)$ can be calculated from the above differential cross–sections by making measurements of both the parallel/anti–parallel and perpendicular/anti–perpendicular scattering rates in a DIS experiment. The details of the manipulation are shown in equations 10 through 13.

While there is no *a priori* determination of a particular structure function, spin–independent or spin–dependent, there is a rigorous prediction that relates the integral of the difference of the proton spin structure function and the neutron spin structure function. This is known as the Bjorken Sum Rule[?]

$$\lim_{Q^2\to\infty}\int_0^1 \left(g_1^p(x) - g_1^n(x)\right)\, dx = \frac{1}{6}|g_A|, \tag{7}$$

where $g_A = -1.2573 \pm 0.00281$ is the axial–vector coupling for neutron beta decay.[?] It is important to note that the integral is over the full range of x and that the integral should be evaluated at *infinite* Q^2. Calculable QCD corrections must be applied[?] at finite Q^2.

Ellis and Jaffe[?] proposed that the strange quark sea would be unpolarized

$$\int_0^1 (s^{\uparrow}(x) - s^{\downarrow}(x))dx = 0 \tag{8}$$

and thus introduced the Ellis–Jaffe sum rule for the nucleon

$$\lim_{Q^2\to\infty}\int_0^1 g_1^{p(n)}(x)\, dx = (\pm)\frac{1}{12}g_A\left[1(\pm)\frac{5}{3}\frac{3F-D}{F+D}\right] \tag{9}$$

Again, g_A comes from neutron beta decay, while F and D are constants of hyperon decay.[?] Originally only the spin–dependent structure functions of the proton were measured by the E80 collaboration[?] and E130 collaboration.[?] Data from both of the original SLAC experiments were consistent with the Ellis–Jaffe sum rule for the proton. In 1989 the EMC collaboration presented data consistent with a violation of the Ellis–Jaffe sum rule.[?] Subsequent experiments, both at CERN[?,?] and SLAC[?,?,?] have also shown that the Ellis–Jaffe sum rule is violated[2]. Figure 2 shows some of the world's data for the proton spin structure function.

Once neutron spin–dependent structure functions became available, tests of the Bjorken Sum Rule by the SMC[?] and SLAC–E143[?] collaborations[3] were possible. Summaries of both the Ellis–Jaffe sum rule tests and the Bjorken sum rule tests are shown in Table 1.

[2] Indeed a more careful QCD based analysis results in the quark sea being polarized.[?,?]

[3] The SLAC experiment E142 made the first measurement of the neutron spin structure function

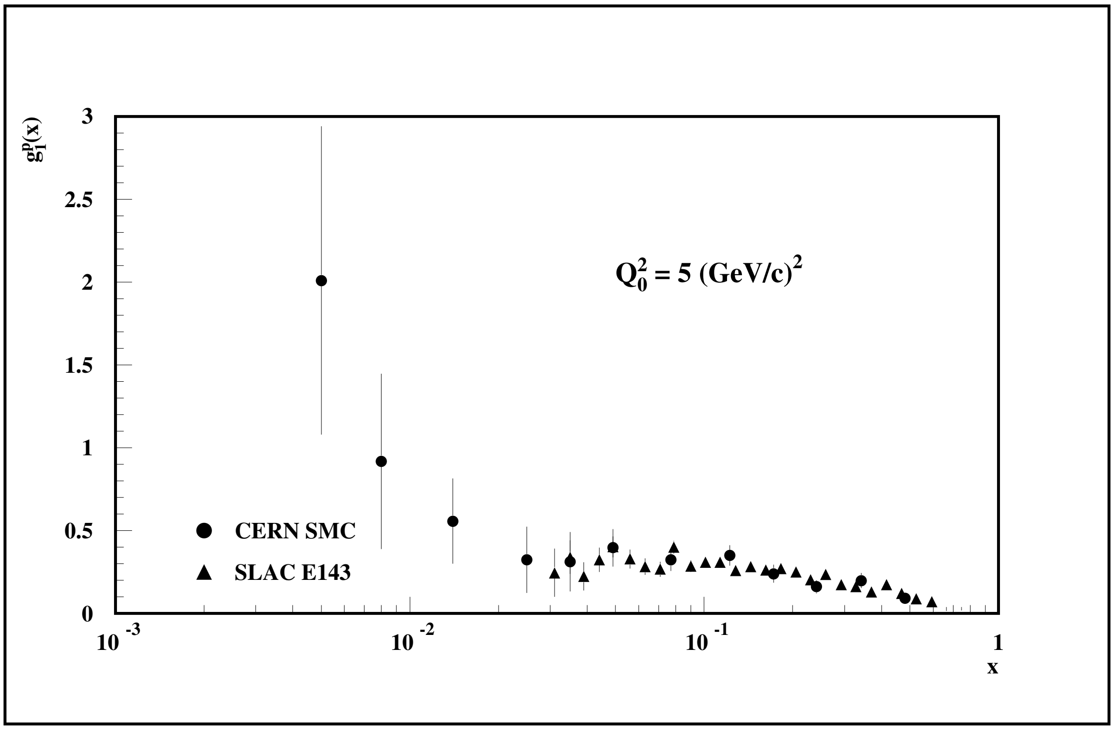

Fig. 2. Some of the currently published data for $g_1^p(x)$. Plotted is $g_1^p(x)$ as a function of x. The data were evolved to $Q_0^2 = 5$ (GeV/c)^2 using Eq. ??.

The amount of published world data for the neutron spin structure function $g_1^n(x)$ is limited due to the difficulty in preparation of an effectively polarized neutron target. To date only the SMC collaboration, SLAC E142, and SLAC E143 have published neutron data[4]. Figure 3 summarizes these data[5]. Naively, the proton structure function appears well behaved in the low–x region ($x < 0.1$). However, the neutron data are not as precise as the proton data in this low–x region. For tests of the Bjorken sum rule, collaborations have assumed two things about the data: a) that the quantity $g_1(x)/F_1(x)$ is Q^2 independent, and b) that the low–x region not covered by data would assume a Regge–like form[?] resulting in $g_1^n(x) \sim$ constant. These two assumptions have been used to extrapolate the

---

$g_1^n(x)$ using a laser–polarized ^{3}He target, however a test of the Bjorken Sum Rule would require use of either the SMC proton data or the SLAC E143 proton data. Both SMC and E143 measured the proton and the neutron spin structure functions $g_1^p(x)$ and $g_1^n(x)$.

[4]Currently an experiment at DESY by the HERMES collaboration has collected neutron spin structure function data with a polarized ^{3}He target, though the statistics are limited with respect to the current experiment.

[5]The shaded region in the figure indicates the kinematic coverage of the current experiment.

(a)	Ellis–Jaffe Sum (proton)	Prediction	Collaboration
	$0.126 \pm 0.010 \pm 0.015$	0.189 ± 0.005	EMC[?]
	$0.049 \pm 0.044 \pm 0.032$	0.187 ± 0.010	SMC[?] (deuteron)
	$0.136 \pm 0.011 \pm 0.011$	0.176 ± 0.006	SMC[?]
	$0.127 \pm 0.004 \pm 0.010$	0.160 ± 0.006	SLAC E143[?]
	$-0.031 \pm 0.006 \pm 0.009$	-0.011 ± 0.016	SLAC E142[?] (neutron)
(b)	Bjorken Sum	Prediction	Collaboration
	0.204 ± 0.029	0.185 ± 0.004	SMC[?]
	$0.163 \pm 0.010 \pm 0.016$	0.171 ± 0.008	SLAC E143[?]

Table 1. (a) Ellis–Jaffe Sum Rule tests and (b) Bjorken Sum Rule tests.

structure functions below the measured regions for the purpose of integrating the structure functions over the full x range. With the advent of precise data such an extrapolation method can be tested as can possibly the Q^2 dependence of $g_1(x)$.

2 Methodology

To precisely measure the neutron spin structure function $g_1^n(x)$ many systematic effects must be well understood. These are summarized in Table 2. This contribution will address the *E154 Experimental Systematics* while the reader is referred to the literature for the best measurements of $F_1(x)$,[?] R,[?] and $g_1^p(x)$.[?,?,?]

E154 Experimental Systematics		
Beam Flux Stability	Beam Polarization	
Target Dilution Factor	Target Polarization	
Electron identification	Background Subtraction	
Radiative Corrections		
External Systematics		
$F_1(x)$	R	$g_1^p(x)$

Table 2. Sources of Systematic Errors

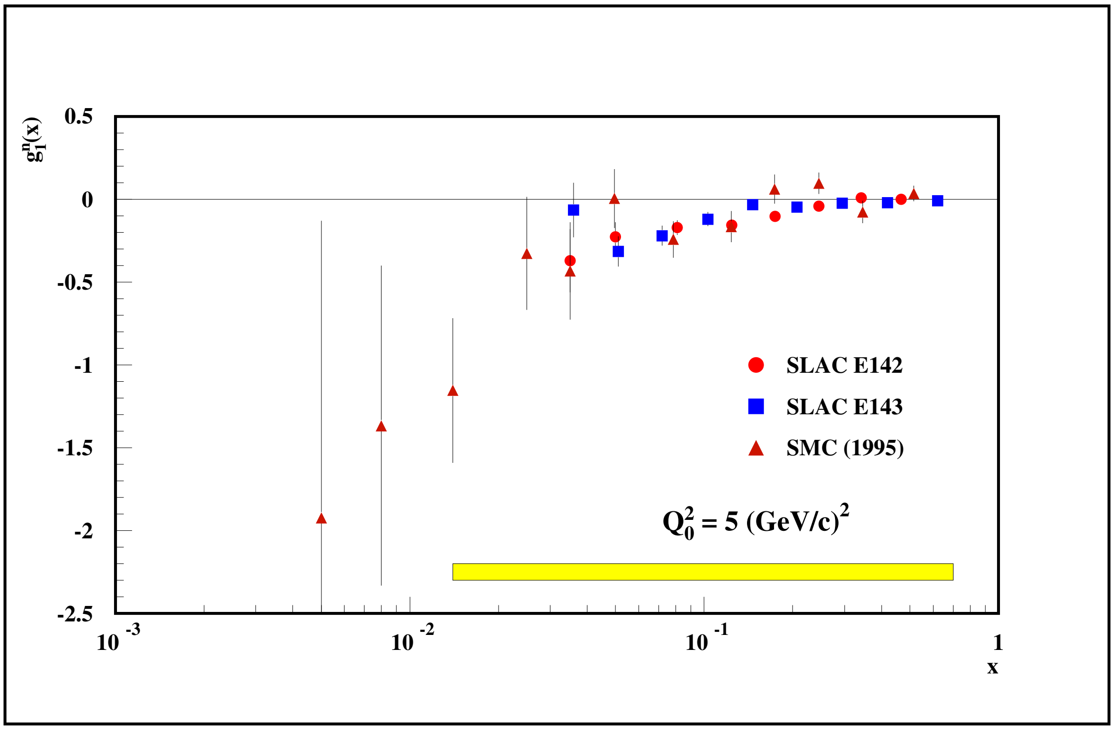

Fig. 3. Published data for $g_1^n(x)$. The shaded region indicates the x interval of the present experiment.

2.1 Cross–sections or ratio of rates

To extract the spin–dependent structure functions either the absolute differential cross–sections must be measured or the asymmetry must be measured. The cross–section and asymmetry measurements are subject to different systematic errors. The advantage of the asymmetry measurement is that experimental conditions such as the spectrometer acceptance drops out in the ratio. Though eventually the absolute DIS cross–section must be known, the value may be taken from precise measurements due to other experiments. The following equations illustrate the latter method.

First we define some variables related to the experimental observables in Table 3. The explicit spin dependence is dropped for brevity. Additionally, the differential cross–sections have implicit x and Q^2 dependence. The acceptance $\mathcal{A}$ in general is also a function of x and Q^2. Finally the dilution factor f is a function of x and Q^2.

We can define the following two ratios, which we shall call the parallel, $A_{\|}$,

n	density of target	l	target length
$\mathcal{A}$	acceptance of spectrometer	F^e	electron beam flux
$d\sigma$	differential cross–section	N^e	observed scattering rate
P_e	electron beam polarization	$P_{^3\mathrm{He}}$	target polarization
f	dilution factor	η	generic efficiency variable

Table 3. Experimental variables

and perpendicular, $A_\perp$, asymmetries

$$\begin{aligned} A_\parallel &= \frac{d\sigma(\downarrow\Uparrow - \uparrow\Uparrow)}{d\sigma(\downarrow\Uparrow + \uparrow\Uparrow)} \\ A_\perp &= \frac{d\sigma(\downarrow\Leftarrow - \uparrow\Leftarrow)}{d\sigma(\downarrow\Leftarrow + \uparrow\Leftarrow)} \end{aligned} \qquad (10)$$

The electron spin directions are denoted by $\uparrow$ and $\downarrow$, while the nuclear spin directions are shown by $\Uparrow$ and $\Leftarrow$. The experiment is able to measure these ratios by observing the scattering rates as a function of beam polarization state. A given rate can be expressed as

$$N^e = F^e \; n \; l \; \mathcal{A} \; \eta \; d\sigma \qquad (11)$$

Since the beam polarization (P_e) and target polarization ($P_{^3\mathrm{He}}$) are in general not 100% and the ^{3}He gas is confined to a glass target vessel, the observed rates relate to the parallel and perpendicular asymmetries according to

$$A_\parallel = \frac{1}{P_e \; P_{^3\mathrm{He}} \; f \; \eta'} \; \frac{N^e_{\downarrow\Uparrow}/F^e_\downarrow - N^e_{\uparrow\Uparrow}/F^e_\uparrow}{N^e_{\downarrow\Uparrow}/F^e_\downarrow + N^e_{\uparrow\Uparrow}/F^e_\uparrow} \qquad (12)$$

where η' represents efficiencies that do not necessarily cancel in the ratios[6] and f is the dilution factor defined in section 2.5. A similar expression exists for the perpendicular asymmetry. Manipulation of equation 4 along with the definition of the asymmetries in equation 10 and the equations that relate the asymmetries to experimental observerables such as equation 12 then lead to the structure functions $g_1(x)$ and $g_2(x)$

$$\begin{aligned} g_1(x) &= \frac{F_1(x)}{D}\left[A_\parallel + \tan\left(\frac{\theta}{2}\right) A_\perp\right] \\ g_2(x) &= \frac{y\;F_1(x)}{2\;D}\left[\frac{E + E'\cos(\theta)}{E'\sin(\theta)} A_\perp - A_\parallel\right] \;, \end{aligned} \qquad (13)$$

[6]Such as any efficiencies that are dependent upon rate. If such efficiencies exist then they will become dependent upon the asymmetry being measured.

D and y are kinematic factors defined by

$$
\begin{aligned}
y &= \frac{E-E'}{E} & D &= \frac{(1-\epsilon)(2-y)}{y(1+\epsilon R)} \\
\epsilon &= \left[1+2(1+\nu^2/Q^2)\tan^2(\frac{\theta}{2})\right]^{-1} & R &= \frac{\sigma_0}{\sigma_T}
\end{aligned} \tag{14}
$$

Finally, because the spin of the neutron in the ^{3}He nucleus is not 100% aligned with the nuclear spin, and because the protons have a residual polarization the neutron spin structure function $g_1^n(x)$ takes the form

$$g_1^n(x) = \frac{1}{P_n}\left(g_1^{^3\mathrm{He}}(x) - 2\ P_p\ g_1^p(x)\right) \tag{15}$$

with $P_p = -0.027$ and $P_n = 0.87$.

2.2 Experimental description

Two small acceptance magnetic spectrometers ($d\Omega \sim$ 5msr) were used to observe deep inelastic scattering rates of 48.3 GeV polarized electrons impinging on a gaseous laser–polarized ^{3}He target. Approximetely 100 million events were collected over a period of two months (October and Novemeber of 1995) at the Stanford Linear Accelerator Center. The experiment ran in fixed target hall End Station A. The majority of the events were collected in a polarization configuration in which the beam was polarized along the direction of the beam axis and the target was polarized along the same axis. The asymmetry in this configuration of polarization vectors is dominated by the spin structure function $g_1^n(x)$. With the target polarization perpendicular to the electron beam, the asymmetry is dominated by other spin structure function[7] $g_2^n(x)$. As previsously stated this talk only presents results on the measurement of $g_1^n(x)$.

2.3 electron beam

The electron beam originates at the polarized electron source.[?] This source utilizes a strained–lattice GaAs crystal in conjunction with a Ti–Sapphire laser system. Illumination of the strained crystal with a particular helicity of the laser light produces a current of highly polarized electrons which are accelerated to an energy of 48.3 GeV. The laser light was applied in a pulse mode, each pulse

[7] Todd Averett for the E154 collaboration, SPIN 96 Proceedings, Amsterdam, The Netherlands.

being $200-250$ns long. The helicity of the laser light was determined by the high voltage applied to two Pockels cells. For the present experiment the helicity state of the laser for each pulse was determined by a random number generator. By doing this random flipping of the beam polarization flucuations in beam flux and experimental acceptance and efficiencies were averaged and thus systematic errors were reduced.

$$\begin{aligned} < \mathcal{A}_{\uparrow} > &= < \mathcal{A}_{\downarrow} > \\ < \eta_{\uparrow} > &= < \eta_{\downarrow} > \end{aligned} \qquad (16)$$

For the experiment we utilized a beam current between $3 \cdot 10^9$ and $9 \cdot 10^9$ electrons per pulse. The accelerator provided 120 pulses per second, though 1 pulse was used to monitor accelerator performance. The beam polarization was measured in dedicated runs using a single arm Möller polarimeter.[?] Average beam polarization was stable at 0.825 and was measured with less than a 5% relative error. Off–line analysis cuts were used to prepare parent samples of DIS events which had beam flux distributions identical to better than 10^{-4}. Analysis examined both spatial and charge distributions of the pulses.

2.4 ^{3}He polarized target

To measure the neutron spin structure function $g_1^n(x)$ the experiment E154 chose to use a spin–exchange ^{3}He gaseous target[8]. The experiment utilized a sealed two cell target system. The target system is schematically shown in Figure 4. An upper cell was used for laser optical pumping of a Rb vapor. Rubidium density was controlled by heating the upper cell to $\sim 180^\circ$ C. Circularly polarized light provided by 3 solid state laser diode arrays and 4 Ti–Sapphire lasers illuminated the upper cell. This results in an atomically polarized Rb vapor. The Rb vapor and the ^{3}He gas freely diffuse and undergo hyperfine interactions during collisions resulting in polarization transfer from the Rb atomic electron to the ^{3}He nucleus.[?] The ^{3}He polarization is governed by

$$P_{^3\mathrm{He}}(t) = P_{\mathrm{Rb}} \frac{\gamma_{SE}}{\gamma_{SE}+\Gamma} \left(1 - e^{(\gamma_{SE}+\Gamma)t}\right) \qquad (17)$$

where P_{Rb} is the average rubidium atomic polarization, γ_{SE} is the spin–exchange rate between the rubidium and the ^{3}He, and Γ is the intrinsic cell relaxation time.

[8] In contrast to the experiment DESY/HERMES which uses a meta–stability exchange based ^{3}He polarization system.

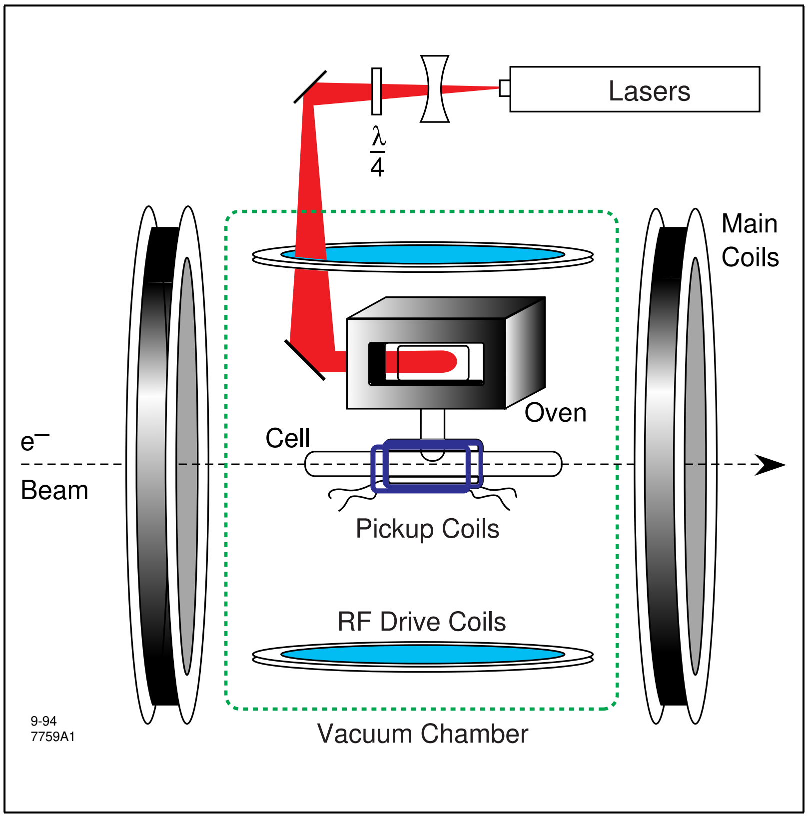

Fig. 4. Schematic of Laser–Polarized ^{3}He Target.

Typical values were $P_{\rm Rb} \sim 0.60$, $\gamma_{SE} \sim 16$ hr^{-1}, and $\Gamma \sim 70$ hr^{-1}. Figure 5 illustrates the atomic levels of the rubidium valence electron and the effect of optical pumping. A quantization axis is achieved with two sets of large helmholtz coils providing a holding field of $10 \sim 20$ gauss. Longitudinal target polarization is set by having the holding field parallel to the beam axis, while a transverse field results in perpendicular polarization[9]. The target cells were filled with ^{3}He to a pressure of approximately 10 atmospheres. Additionally each cell had in it a small amount of N_2 ($\sim$60 torr) to aid in the optical pumping process. The bottom (target) cell through which the high energy electron beam passed was constructed with very thin entrance and exit windows ($\sim 50\ \mu$m). The lower, target, cell was 30 centimeters long. Average target polarization over the the 2 month duration of the experiment was $38\% \pm 2\%$ and as high as 50%. The target polarization was

[9] During perpendicular running of the experiment the target cell was permitted to cool and the lasers were turned off. The ^{3}He polarization was allowed to decay with a time constant on the order of many 10's of hours. This was done because the optical path of the laser light was fixed for parallel pumping only.

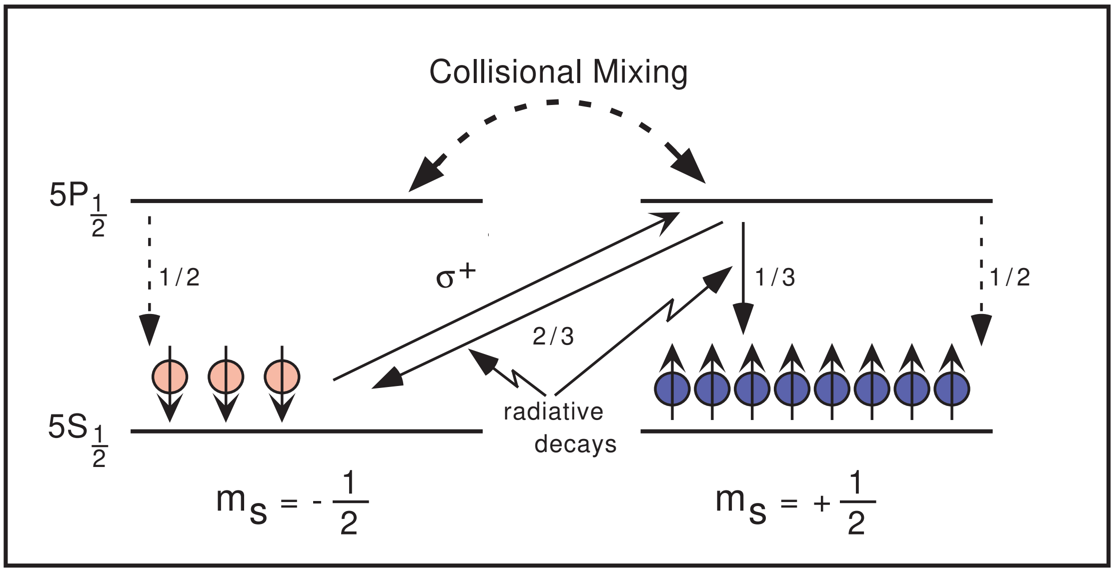

Fig. 5. Optical Pumping of Rubidium. The circularly polarized light is denoted by σ^+. In the abscence of N_2 the $5P_{1/2}$ state deexcites with a ratio of relative rates of 2/3:1/3. Introduction of a small amount of N_2 results in collisional mixing and increases this ratio to 1/2:1/2.

regularly measured throughout the course of the experiment using *adiabatic fast passage*, a NMR technique.[?] The NMR was calibrated by two methods: proton NMR and Rb EPR.[?] In the analysis of the data, the interpolated polarization for each run was used.

2.5 target dilution factor f

The advantages of using a closed optical pumping cell for the nuclear target for DIS is the high densities achieved. However, this results in DIS events originating from nuclei other than the ^{3}He. The ratio of the events from the ^{3}He to the sum of events from all species is referred to as the dilution factor[10] f.

$$f = \frac{N_{\downarrow}^{^3\mathrm{He}} + N_{\uparrow}^{^3\mathrm{He}}}{N_{\downarrow}^{^3\mathrm{He}} + N_{\uparrow}^{^3\mathrm{He}} + (N_{\downarrow}^{\mathrm{N}_2} + N_{\uparrow}^{\mathrm{N}_2}) + (N_{\downarrow}^{\mathrm{glass}} + N_{\uparrow}^{\mathrm{glass}})} \tag{18}$$

In the observed asymmetries, the numerator is only dependent upon the polarized ^{3}He as the glass target vessel and the N_2 gas are unpolarized. However, the

[10] The nuclear spin directions ($\Uparrow$ and $\Leftarrow$) are not shown since this formula holds for all nuclear spin directions.

denominator, which is a measure of the spin–averaged scattering rates is sensitive to the presence of any matter in the electron beam. The ratio of the difference of the spin–dependent scattering rates from ^{3}He to the sum is

$$P_e \; P_{^3\mathrm{He}} \; A_{^3\mathrm{He}} = \frac{N_\downarrow^{^3\mathrm{He}} - N_\uparrow^{^3\mathrm{He}}}{N_\downarrow^{^3\mathrm{He}} + N_\uparrow^{^3\mathrm{He}}} = f \; \frac{N_\uparrow^{\mathrm{Total}} - N_\downarrow^{\mathrm{Total}}}{N_\uparrow^{\mathrm{Total}} + N_\downarrow^{\mathrm{Total}}} \tag{19}$$

Because the glass target vessel is unpolarized as is the N_2 gas the difference in the spin–dependent ^{3}He scattering rates is identical to the difference in the total spin–dependent scattering rates

$$N_\downarrow^{^3\mathrm{He}} - N_\uparrow^{^3\mathrm{He}} = N_\uparrow^{\mathrm{Total}} - N_\downarrow^{\mathrm{Total}} \tag{20}$$

Precise determination of f is crucial to the measurement of $g_1^n(x)$. We used two methods: 1) physical characterization of the target cell with detailed calculation of expected rates from contributions due to different matter present, and 2) use of a variable pressure reference cell to directly measure rates of deep inelastic scattering from ^{3}He.

2.5.1 dilution factor method 1 : calculated with target physical characteristics

In method 1 each target cell was measured to determine the amount of glass in the path of the incoming high energy electron beam. In addition to mechanical measurements of the target windows, thickness determination was done by performing X–ray absorption measurements and using laser–interferometric techniques. The gas density was measured at the time of target manufacture using standard pressure gauges. The gas density was also determined using an optical line broadening technique.[?] This information was used to construct a detailed mathematical model of each target used in the course of the experiment[11]. Published values of nucleon structure functions[?] for the proton and the neutron ($F_2^p(x, Q^2)$ and $F_2^n(x, Q^2)$) along with knowledge of the EMC effect[?] were used in conjuction with internal radiative corrections[12] to calculate deep inelastic scattering rates.

[11]Due to the thinness of the target windows $\sim 50\ \mu$m, the target cell windows had a limited life in the electron beam. Different target cells were used during the course of the experiment.

[12]Initial and final state radiation along with vertex corrections were calculated. Additionally radiative corrections were applied to *elastic scattering* and *quasielastic scattering* to be combined with the radiative corrections of the deep inelastic scattering to calculate an overall *effective* radiative correction to the deep inelastic scattering.

These rates were calculated as distributions of both x and Q^2. Finally these rates were corrected for effects of *external radiation*[13] due to the path of the scattered electrons through the target cell wall and the spectrometer detector components. Final distributions were used to calculate the dilution factor.

2.5.2 dilution factor method 2 : measurements in beam

The second method of dilution factor determination utilized variable pressure ^{3}He reference cells. An advantage of the reference cell method is that the internal and external radiative corrections are included since the cross–sections are physical, to all orders. The variable pressure reference cells were constructed in the same manner as the target cells, with the exception that no optical pumping cell was attached. By recording the scattering rate into each spectrometer as a function of the ^{3}He density in the reference cell, the rate of electrons due to events originating in the ^{3}He and those originating in the glass target windows can be decoupled. This decoupling is illustrated below

$$N^e = F^e\, l_{^3\mathrm{He}}\, n_{^3\mathrm{He}}\, \mathcal{A}\, d\sigma_{^3\mathrm{He}} \;+\; F^e\, l_{\mathrm{glass}}\, n_{\mathrm{glass}}\, \mathcal{A}\, d\sigma_{\mathrm{glass}} \tag{21}$$

where now the density $n_{^3\mathrm{He}}$ is varied by the experimenters. This can be summarized in the following equation.

$$N^3 = \mathcal{M}\; n_{^3\mathrm{He}} + \mathcal{R}_{\mathrm{glass}} \tag{22}$$

The reference cell can be pressurized to various densities and the rate per unit density $\mathcal{M}$ can be measured. Note that this rate variable ($\mathcal{M}$) is explicitly dependent[14] upon x and Q^2. The extracted rate can then be used to construct a dilution factor

$$f = \frac{\mathcal{M}\; \tilde{n}_{^3\mathrm{He}}}{N_{\mathrm{Total\ Rate}}}\ , \tag{23}$$

where $\tilde{n}_{^3\mathrm{He}}$ is the actual operating density of the polarized target while the electron beam is impinging. The total electron scattering rate given by $N_{\mathrm{Total\ Rate}}$ is just the total rate as observed by each spectrometer[15]. Excellent agreement is

[13] The radiative effects were calculated as prescribed by Mo and Tsai[?] and through the use of the monte carlo program GEANT.[?] In the latter method a detailed model of the target was incorporated into the program. Additionally descriptions of the two spectrometers, including magnets, detector elements, vacuum windows etcetera were used.

[14] However, the narrow Q^2 range in any given x bin results in $\mathcal{M}$ being a function of mainly x.

[15] Each spectrometer had a dilution factor calculated using both methods.

found between the two methods of dilution factor determination, as illustrated by Figure 6.

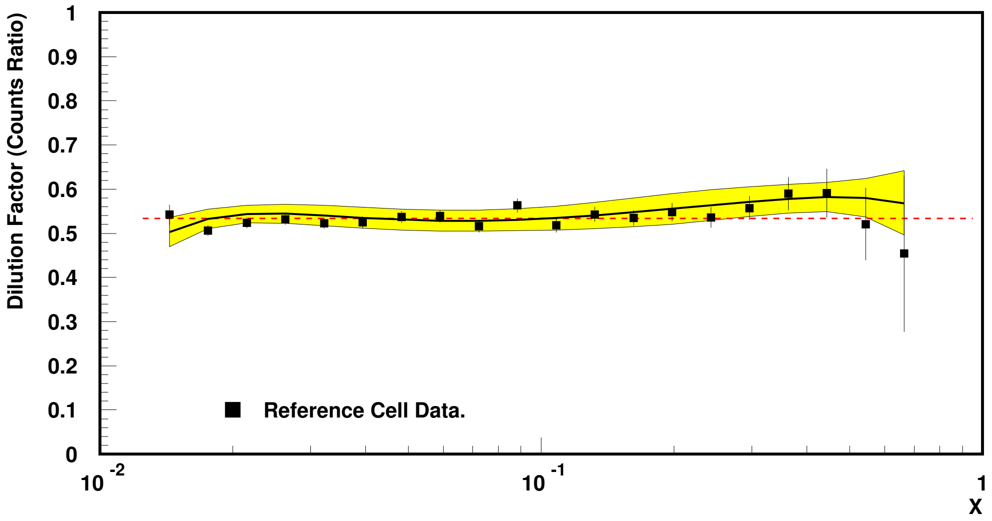

Fig. 6. Dilution factor as determined by mechanical measurement and as determined by reference cell rate measurement (symbols). The band is the result of the calculation based on the parameterization of the cell.

2.6 electron identification and background suppression

The experiment utilized magnetic spectrometers at forward angles[16]. The spectrometers were triggered by every pulse and the electronics were gated for a 400 ns duration. This mode of triggering enabled the experiment to record multiple events in any given pulse. Each spectrometer used magnets for momentum and charge selection of the scattered particles. Each spectrometer had non–vanishing acceptance for electrons above a momentum of 10 GeV/c. The momentum was reconstructed via the use of tracking hodoscopes[17]. The hodoscopes were instrumented with multiple–hit TDC's, thus permitting the recording of multiple events in a pulse. Electron identification was achieved with a combination of

[16]The SLAC experiments E142 and E143 were precursors to the present experiment. A brief description has been published.[?]

[17]Thin fingers of scintillator material paired with a photo–multiplier tube (PMT).

threshold gas Cerenkov detectors and lead–glass shower array detectors. As with the hodoscopes, the lead–glass detectors were also instrumented with multiple–hit TDC's. Each Cerenkov detector was instrumented with a high time resolution (1 nanosecond/bin) Flash ADC. Analysis of the digitized PMT waveforms led to e^- identification and π^- rejection for momentum below 19 GeV/c and 16 GeV/c for the 2.75° and 5.50° spectrometers respectively. Situated at the far end of each spectrometer, as shown in Figure 7, was an array of lead–glass block in the *Fly's Eye* configuration sufficiently long for total containment of e^- (e^+) induced electromagnetic cacades. Particle energy reconstruction was done along with a shower development analysis using a neural network based algorithm. The energy value along with the momentum value were used to construct a ratio. For electrons the ratio would have a mean of 1, while for π^-'s the value would be different and less than 1. Further e^- identification was done by examining the results of the neural network analysis. Thus a final e^- profile could be determined. A complementary analysis also led to π^- profiling. An interplay of the e^- and π^- analyses then led to an efficiency and background rate determination[18].

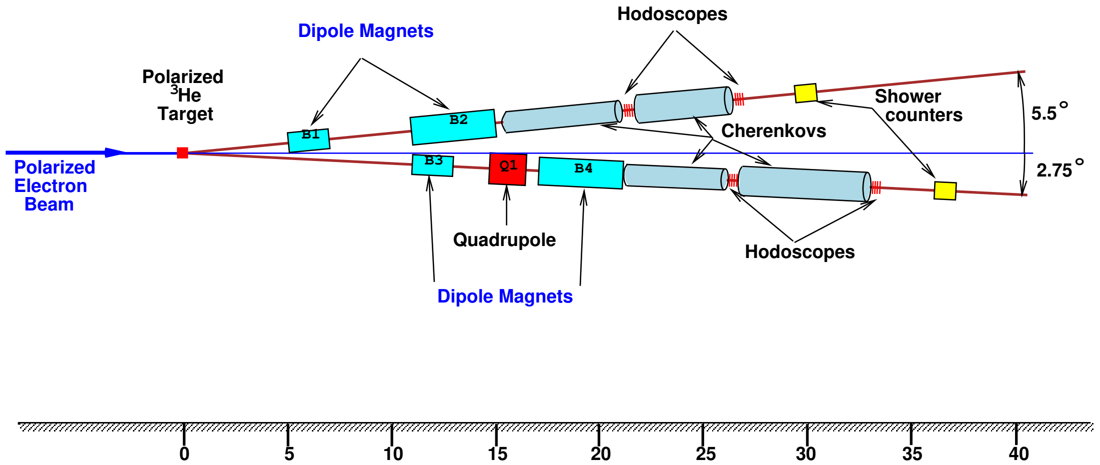

Fig. 7. Schematic of the 2.75° and 5.50° spectrometers as seen from above.

[18]A residual sample of e^- in the final π^- sample and a residual sample of π^- in the final e^- sample are viewed as background contaminations. These background rates were measured to be small.

2.7 radiative corrections

Equation 4 was written in the Born approximation (1 photon exchange). What is actually observed is the cross–section to all orders. In order to extract the spin–dependent structure functions the effects of higher than Born radiation must be taken into account. These corrections are referred to as internal and external radiative corrections. In addition to spin–averaged internal corrections, spin–dependent internal corrections must be calculated.

2.7.1 external radiation

External radiative corrections include energy loss of the electron beam while traversing the target and energy loss of the scattered beams while exiting the target and traversing the detector elements. The incident beam energy loss is neglible in the thin target. Energy loss of the scattered electrons due to traversal through the target and the spectrometer elements can be explicitly calculated given the physical description of all matter encountered in the spectrometer line. In this way each scattered electron can have its momentum corrected to the value just after the initial deep inelastic scattering.

2.7.2 internal radiation

There are two distinct sources of internal radiative corrections. Those that are calculated in the spin–averaged (unpolarized) case and those that are spin–dependent (polarized). Since the experiment measures an asymmetry which is the ratio of spin–dependent and spin–averaged processes both polarized and unpolarized radiative corrections must be calculated. Polarized radiative corrections alone are a subject worthy of discussion at a conference or workshop. To this end the reader is referred to the latest literature on the topic.[?,?] However a brief description is warranted. Angular momentum conservation results in radiative corrections to deep inelastic scattering being different for the spin–dependent case compared to the spin–averaged case. The process of calculating the polarized radiative corrections entails the use of the observed deep inelastic scattering asymmetries. A polarized correction is calculated and applied to the asymmetry. The resulting asymmetry is then used to calculate a new correction. This iterative process is continued until the corrections converge.

3 Experimental Results

The analysis was carried out by two relatively independent sub–groups of the collaboration. This allowed for a study of systematic effects possibly introduced by the analysis methods. The large data sets were analyzed on computer farms at SLAC and at *The California Institute of Technology.* Reduction of the data led to data summary tapes (DST's) with analysis cuts refined for e^- selection. Pion identification has already been discussed in section 2.6, another background is *false* electrons. These are real electrons (not pions) that have an origin other than deep inelastic scattering[19] The observed electrons can be described by

$$N^e_{\mathrm{Total}} = N^e_{True} + N^e_{False}. \tag{24}$$

The *false* electrons have a charge symmetric origin, such as π^0 *Dalitz* decay,

$$\pi^0 \rightarrow \gamma\ e^-\ e^+\ . \tag{25}$$

Other sources would include pair production from high energy γ's. In order to remove these *false* e^-'s the polarity of each spectrometer was periodically reversed to accept positrons. The observed positron rate is a measure of these false electrons. Numerical asymmetries were constructed from the DST files. These were then corrected for π's and *false* e^-'s. Use of the dilution factor, beam polarization, and target polarization then results in the asymmetries $A_{\|}$ and $A_{\perp}$. These asymmetries were then corrected for radiative effects and the spin–dependent structure functions extracted.

Due to the finite acceptance of each spectrometer the structure functions were measured in a range of Q^2 that is highly correlated with x. This correlation of Q^2 and x arises from the fixed angle of each spectrometer and the small entrance apertures. This Q^2 and x acceptance is shown for the two spectrometers in Figure 8. In order to present $g_1(x)$ in a meaningful manner the Q^2 value should be fixed to a common value for all x values. However, because of the acceptence correlation the mean Q^2 values increase as a function of x. Early spin–dependent structure function experiments made explicit check for Q^2 dependence for the ratio of the spin–dependent structure function to the spin–averaged structure function.[?] To

[19] In addition to deep inelastic scattering, radiated elastic and radiated quasielastic scattering are included in the definition of *true* electrons since these are accounted for in the radiative corrections.

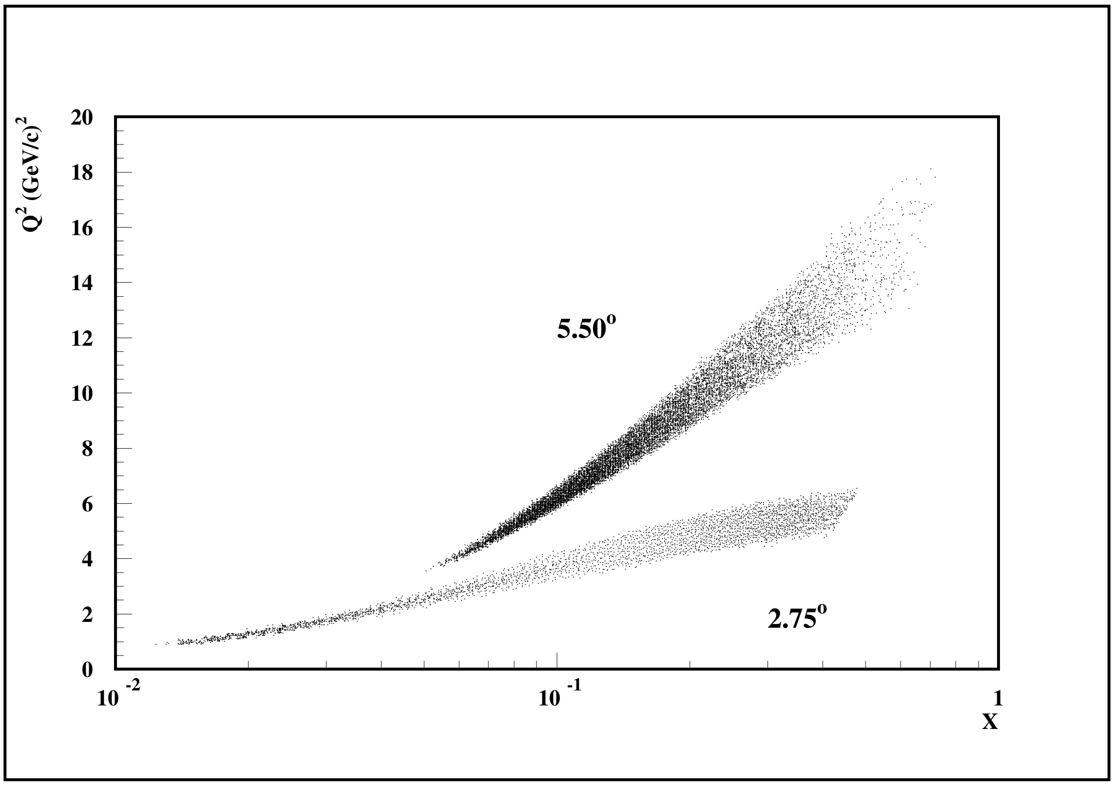

Fig. 8. Acceptance Map of the 2.75° and 5.50° Spectrometers in Q^2 and x.

the statistical and systematic precision of the experiment no significant Q^2 dependence was found. That is

$$\left.\frac{g_1(x,Q^2)}{F_1(x,Q^2)}\right|_{x=x'} = \text{constant}\ . \tag{26}$$

Assuming validity of this relationship, the structure function $g_1^n(x,Q^2)$ can be evolved to a mean Q_0^2 to arrive at $g_1^n(x,Q_0^2)$. We chose to evolve to the average Q^2 observed in the data[20], namely $Q_0^2 = 5$ (GeV/c)^2. Figure 9 shows the results of our experiment. The precision of the data is striking. An important feature of the data is the increase in the structure function at lower values of x. This is a possible indication of near divergent behavior of the structure function.

The data need to be evolved to a common Q^2 value in order to compare the current data to the world data for $g_1^n(x)$. Equation 26 was used to evolve the world data to the average Q^2 of 5 (GeV/c)^2. The results of this evolution are shown in Figure 10. Additionally, the product $xg_1^n(x)$ as a function of x is shown rather than $g_1^n(x)$. This method of data presentation allows for a clearer comparison of

[20] This is the current convention used by spin–dependent structure function experiments.

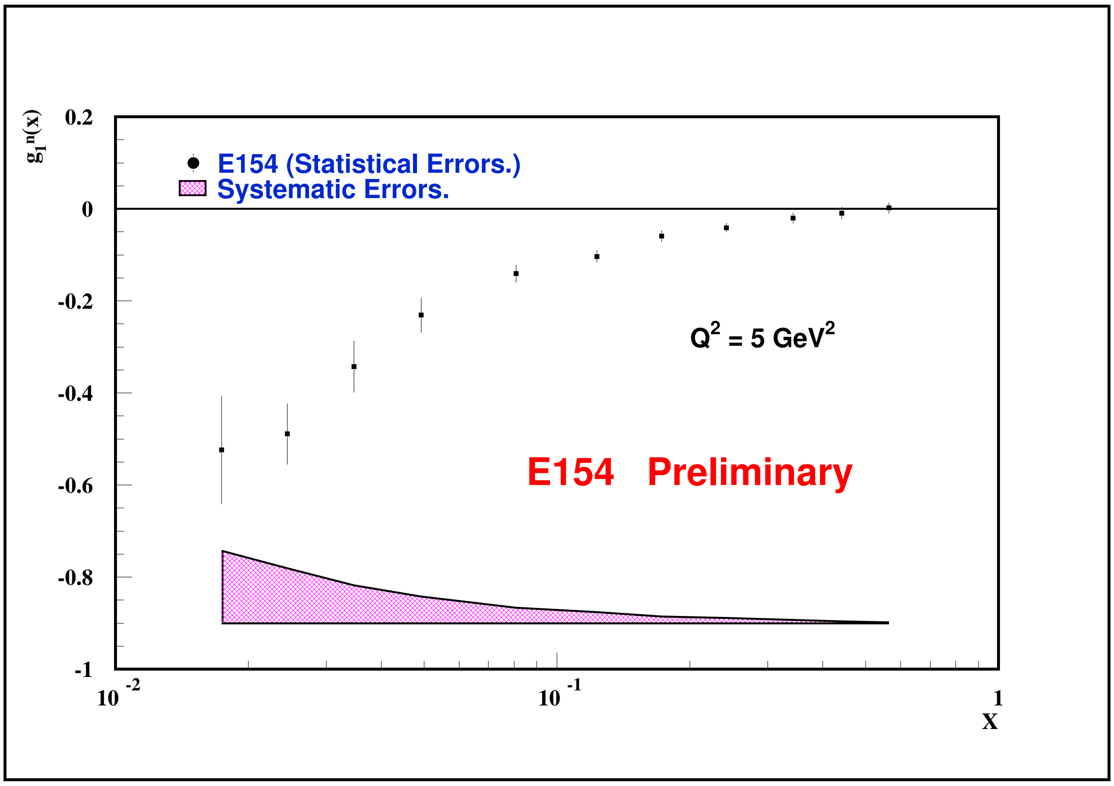

Fig. 9. Results of E154 measurement of the neutron spin structure function $g_1^n(x)$ evolved to a mean Q^2 of 5 $(\mathrm{GeV/c})^2$. The error bars are statistical only. The band near the bottom of the plot is the 1 σ systematic error.

experiments, an appreciation of the precision of each experiment, and a sense of the convergence of $\int_0^1 g_1^n(x)dx$. The precision of the current data in comparison to the world data can not be overstated.

The numerical integral over the covered data range is

$$\int_{0.014}^{0.70} g_1^n(x)\ dx = -0.036 \pm 0.004(\text{statistical}) \pm 0.005(\text{systematic}) \tag{27}$$

In order to integrate over the full x range extrapolations below and above the covered data range must be done. For the high x region quark–counting arguments[?] may be followed that lead to an extrapolation of the form

$$g_1^n(x) \to (1-x)^3 \tag{28}$$

This form leads to a small contribution to the overall integral

$$\int_{0.70}^{1.0} g_1^n(x)dx \sim 0.0002 \tag{29}$$

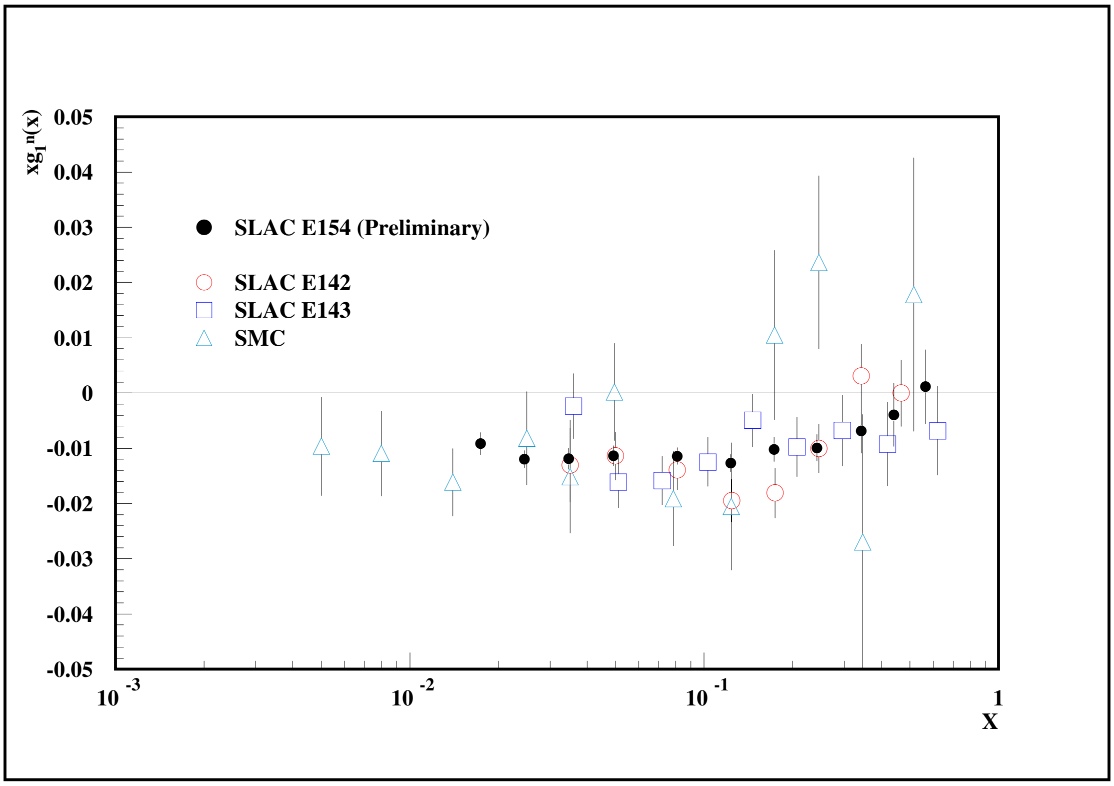

Fig. 10. Comparison of results of E154 and the rest of the world for the spin structure function $g_1^n(x)$ evolved to a common Q^2 of 5 (GeV/c)^2. Evolution is done with Eq. ??.

The low–x behavior is, however, another matter. Since the data show an increase at low values of x the extrapolation is more tenuous. The precision of the data brings into question the validity of naive low–x extrapolation models, such as the Regge–like behavior.

$$g_1(x) \sim x^{\alpha} \ . \tag{30}$$

Under the constraint that the exponent α in the Regge inspired model is required to assume a value in the range $0 \leq \alpha \leq 0.5$, the best fit in the low–x ($x < 0.1$) interval of neutron data leads to an exponent of $\alpha = 0$. However, if the exponent is allowed to assume any value the fit leads to near divergent behavior. The two vastly different fits indicate the complexity of extrapolating.

The isovector difference in the structure functions is solely non–singlet and is expected to have softer behavior.[?] Under this premise the difference in structure functions takes the form

$$(g_1^p(x) - g_1^n(x)) \rightarrow C\ x^{\alpha} \tag{31}$$

A combination of the SMC and E143 proton data may be taken along with the present neutron data to construct the difference. All points below $x < 0.1$ are used to calculate the fit parameters. The resulting fit is shown in Figure 11. With this extrapolation, the form may be integrated and a Bjorken sum rule value

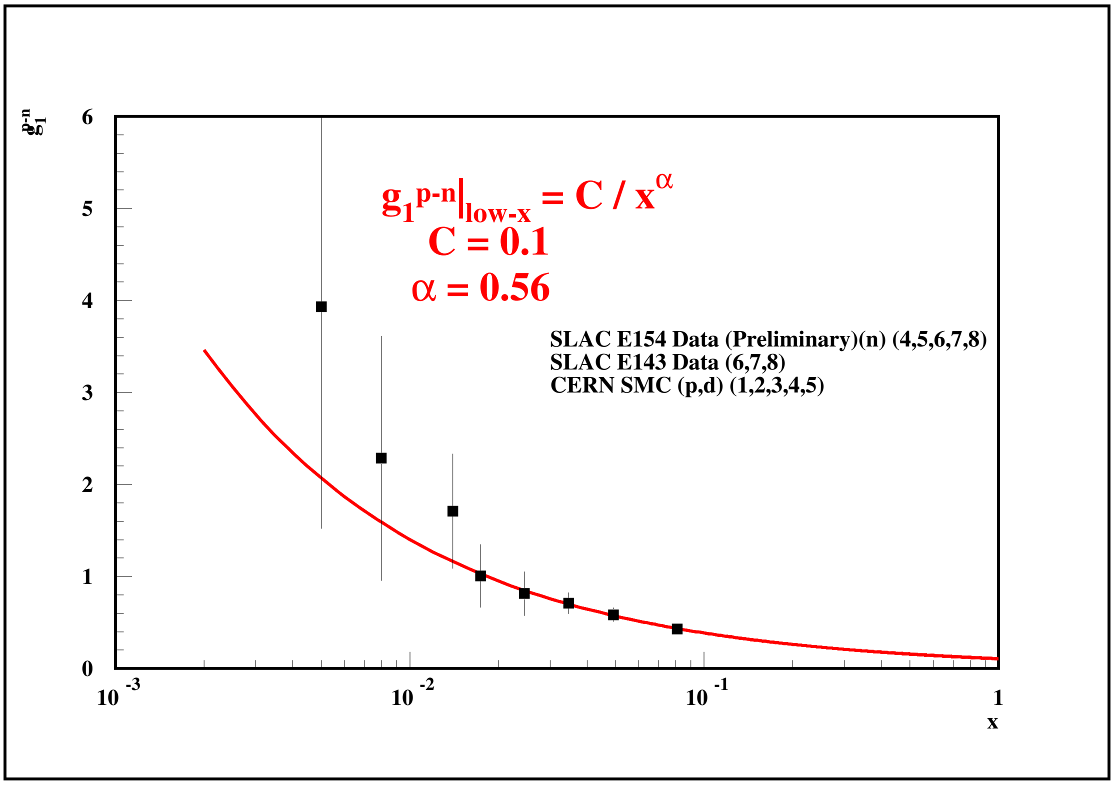

Fig. 11. Power Law fit to $g_1^p(x) - g_1^n(x)$ in the low–x region using proton data from SMC and E142 along with neutron data of E154. For the x–region below the kinematic region of E154 the SMC data alone were used to construct $g_1^p(x) - g_1^n(x)$.

calculated. In order to estimate the systematic error involved in the extrapolation, the fit can be done with and without the inclusion of the quantity $g_1^p(x) - g_1^n(x)$ below the E154 data range of $0.014 < x < 0.70$. The low–x extrapolation results in the following integral

$$\int_{0.0}^{0.014} (g_1^p(x) - g_1^n(x))dx = 0.041 \pm 0.007 \tag{32}$$

The average of the two extrapolations is taken as the integral and half the difference is taken as an estimate of the extrapolation error. Due to the preliminary nature of the data, the Bjorken Sum Rule calculated here is viewed as more a qualitative check rather than a high precision test. Evolution of the available data on the proton spin structure function leads to a global phenomenological fit resulting in an integral over the finite x range of

$$\int_{0.014}^{1.0} g_1^p(x)dx = 0.121 \pm 0.004 \pm 0.008 \tag{33}$$

Use of the high–x extrapolation found in equation 28 and the measured data range of the present experiment gives the neutron contribution in the same x region of

$$\int_{0.014}^{1.0} g_1^n(x)dx = -0.036 \pm 0.004 \pm 0.005 \tag{34}$$

These evaluations along with the low–x extrapolation on the difference of the structure functions gives a value of the Bjorken Sum Rule of

$$\int_0^1 (g_1^p(x) - g_1^n(x))dx = 0.198 \pm 0.006 \pm 0.011 \tag{35}$$

Consistent with the current Q^2 value of 5 (GeV/c)^2 the $O(\alpha_s^3)$ QCD corrected calcuation of the Bjorken Sum Rule is

$$\int_0^1 (g_1^p(x) - g_1^n(x))dx = 0.181 \pm 0.003 \tag{36}$$

Certainly the statistical precision of the available data is sufficient to test the Bjorken Sum Rule, however, the uncertainty in the extrapolation to low–x values ($x \rightarrow 0$) is high. Even though the low–x fit results in a reasonable value of χ^2/D.F. the assumptions of the extrapolation form might not be valid.

4 Conclusions

The experiment E154 has provided the scientific community with the most precise measurement of $g_1^n(x)$ in the kinematic range of $0.014 \leq x \leq 0.70$. An associated collaboration, E155, will be finished with a complementary set of high precision $g_1^p(x)$ and $g_1^d(x)$ data in the sping of 1997. The experiment E155 will be using the same spectrometers with minor improvements. Additionally a new spectrometer[?] has been constructed to detect scattered electrons at the angle of 10.5°. This will result in a data set that spans a much wider Q^2 range for a given value of x. By themselves, the high precision results of E154 have brought into question the past methodology of handling extrapolations of the spin–dependent structure functions to regions in x below that which has been covered by experiments. Recent theoretical work in perturbative QCD has resulted in evolution equations in

Next–to–Leading–Order for the spin–dependent structure functions which can be used to analyze the experimental data.[?,?] This manner of analysis should result in more reliable extrapolations to low–x regions and provide for an indirect measurement of the gluon angular momentum contribution to the spin of the nucleon. Until direct measurements of low x is undertaken this will be the only method by which to probe the low–x realm of the spin–dependent structure functions. Such experiments will need the devolopement of a new electron–nucleon colliding facility. The proposed *Next Linear Collider* could be such a facility; or low x could be probed by polarizing the protons at the collider facility at DESY. Spin–dependent gluon structure functions have yet to be directly measured, however experiments at the *Relativistic Heavy Ion Collider* (RHIC) at Brookhaven National Laboratory are in preparation in which polarized protons will collide with polarized protons.